AGU ADVANCING EARTH AND SPACE SCIENCE

Earth and Space Science

RESEARCH LETTER
10.1029/2021EA001839

Special Section:
The Ice, Cloud and land Elevation Satellite-2 (ICESat-2) on-orbit performance, data discoveries and early science

New Ocean Subsurface Optical Properties From Space Lidars: CALIOP/CALIPSO and ATLAS/ICESat-2

Xiaomei Lu[1,2], Yongxiang Hu[2], Yuekui Yang[3], Thomas Neumann[3], Ali Omar[2], Rosemary Baize[2], Mark Vaughan[2], Sharon Rodier[1,2], Brian Getzewich[2], Patricia Lucker[1,2], Charles Trepte[2], Chris Hostetler[2], and David Winker[2]

[1]Science Systems and Applications, Inc., Hampton, VA, USA, [2]NASA Langley Research Center, Hampton, VA, USA, [3]NASA Goddard Space Flight Center, Greenbelt, MD, USA

Abstract Remote sensing from Earth-observing satellites is now providing valuable information about ocean phytoplankton distributions. This paper presents the new ocean subsurface optical properties obtained from two space-based lidars: the Cloud-Aerosol Lidar with Orthogonal Polarization (CALIOP) aboard the Cloud-Aerosol Lidar and Infrared Pathfinder Satellite Observations satellite and the Advanced Topographic Laser Altimeter System (ATLAS) aboard the Ice, Cloud, and land Elevation Satellite-2 satellite. Obtaining reliable estimates of subsurface biomass necessitates removing instrument artifacts peculiar to each sensor, that is, polarization crosstalk artifacts in the CALIOP signals and after pulsing effects arising from the ATLAS photodetectors. We validate the optical properties derived from the corrected lidar backscatter signals using MODerate-resolution Imaging Spectroradiometer ocean color measurements and autonomous biogeochemical Argo float profiles. Our results support the continued use of present and future spaceborne lidars to study the global plankton system and characterize its vertical structures in the upper ocean.

Key Points:

- Global ocean subsurface properties are retrieved from Cloud-Aerosol Lidar with Orthogonal Polarization (CALIOP)
- The CALIOP crosstalk artifact and Advanced Topographic Laser Altimeter System (ATLAS) after pulsing effects are removed
- High vertical resolution of ocean subsurface profiles can be obtained from ATLAS/Ice, Cloud, and land Elevation Satellite-2

Supporting Information:

Supporting Information may be found in the online version of this article.

Correspondence to:

X. Lu and Y. Hu,
xiaomei.lu@nasa.gov;
yongxiang.hu-1@nasa.gov

Citation:

Lu, X., Hu, Y., Yang, Y., Neumann, T., Omar, A., Baize, R., et al. (2021). New ocean subsurface optical properties from space lidars: CALIOP/CALIPSO and ATLAS/ICESat-2. *Earth and Space Science*, *8*, e2021EA001839. https://doi.org/10.1029/2021EA001839

Received 6 MAY 2021
Accepted 14 SEP 2021

1. Introduction

Ocean color remote sensing entered a new era with the launch of the National Aeronautics and Space Administration (NASA) Coastal Zone Color Scanner in 1978 (C. W. Sullivan et al., 1993). For the first time, maps of phytoplankton biomass (chlorophyll)—a key measurement of marine ecosystems—could be produced from space-based observations, with the potential for daily to interannual observations at ocean basin scales. Regional to global maps of phytoplankton chlorophyll and other products derived from satellite measurements of water-leaving radiance are now accessible to users all over the world and have become an essential tool for the study and analysis of ocean biogeochemistry and ocean ecosystems. For decades, ocean color remote sensing has led to unprecedented scientific understanding in global ocean biology and biogeochemistry (Blondeau-Patissier et al., 2014; Brown et al., 1985; Dickey et al., 2006). However, because previous ocean color measurements have relied solely on passive remote sensing techniques, the data coverage is limited to the uppermost portion of the water column and is unable to resolve the underlying vertical structure (Hostetler et al., 2018; Jamet et al., 2019). Moreover, passive sensors (e.g., the MODerate-resolution Imaging Spectroradiometer, MODIS) only provide ocean color records during daytime. As a result, vast ocean areas in high latitudes during polar nights remain unsampled and places for which data are available typically provide information for only a few months in each calendar year.

Estimates of global phytoplankton distributions from a space-based lidar were first demonstrated using measurements from the Cloud-Aerosol Lidar with Orthogonal Polarization (CALIOP) (Behrenfeld et al., 2013). CALIOP is a dual-wavelength (532 and 1,064 nm), polarization sensitive (at 532 nm) elastic backscatter lidar that has been making measurements from the Cloud-Aerosol Lidar and Infrared Pathfinder Satellite Observations (CALIPSO) satellite since June 2006 (Hunt et al., 2009; Winker et al., 2009). Using the CALIOP depolarization ratio measurements at 532 nm together with colocated A-Train measurements, such as Advanced Microwave Scanning Radiometer-Earth observing system (AMSR-E) wind speeds and MODIS diffuse attenuation coefficients (k_d, m^{-1}), innovative retrieval methods have been developed to translate the CALIOP ocean backscattered signals into ocean optical properties, such as the particulate backscatter coefficient (b_{bp}, m^{-1}) (Behrenfeld et al., 2013; Churnside et al., 2013; Lacour et al., 2020; Lu et al., 2016), phytoplankton biomass (Behrenfeld et al., 2017), and the total depolarization ratio of ocean

waters (Dionisi et al., 2020; Lu et al., 2014). However, CALIOP's coarse vertical resolution (30 m in the atmosphere, 22.5 m in the water) (Behrenfeld et al., 2013; Lu et al., 2014) and the nonideal transient response of the 532 nm detectors (Y. Hu et al., 2007; Lu et al., 2018; Lu, Hu, Vaughan, et al., 2020) present substantial challenges in retrieving ocean subsurface profiles directly from CALIOP measurements.

On September 15, 2018, the Ice, Cloud, and land Elevation Satellite-2 (ICESat-2) mission launched from the Vandenberg Air Force Base, CA carrying the Advanced Topographic Laser Altimeter System (ATLAS) (Markus et al., 2017). ATLAS is a 532 nm photon-counting laser altimeter with a 10 kHz pulse repetition rate and a footprint diameter of 11 m at the Earth's surface (Magruder & Brunt, 2018; Magruder et al., 2020; Markus et al., 2017). The ATLAS instrument architecture differs significantly from CALIOP, allowing it to overcome many of CALIOP's subsurface measurement deficiencies. Our collaborative team onsite at NASA's Langley Research Center and Goddard Space Flight Center has derived a set of new ocean data products from ATLAS/ICESat-2 measurements (Lu et al., 2019; Lu, Hu, Yang, et al., 2020), which, for the first time, quantify the vertical distribution of phytoplankton optical properties below the ocean surface from space. The vertical structure of these subsurface optical properties is not available in the existing ocean color record generated from passive remote sensing measurements (Hovis et al., 1980); hence, the ATLAS/ICESat-2 ocean results provide unique new information that augments existing ocean color measurements by adding the depth dimension with high horizontal and vertical resolution measurements during both day and night.

Here, we focus on retrieving ocean subsurface optical properties using both CALIOP and ATLAS measurements. For both systems, measurement artifacts such as CALIOP's polarization crosstalk (Lu, Hu, Omar, et al., 2021) (Text S1) and the ATLAS's after-pulsing effects (Lu, Hu, Yang, et al., 2021) (Text S2) are removed in order to obtain reliable ocean subsurface results. The cross-polarization component of the ocean subsurface backscatter (β_{w+}, sr^{-1}), subsurface depolarization ratio (δ_{sub}), and particulate backscattering coefficient (b_{bp}, m^{-1}) are retrieved globally from the CALIOP version 4.1 level 1b (L1) data product (Getzewich et al., 2018; Kar et al., 2018). We use ATLAS geolocated photon data of ATL03 Release 003 (Neumann et al., 2020) to quantify the vertical distribution of ocean subsurface properties (Lu et al., 2019; Lu, Hu, Yang, et al., 2020), such as the profiles of subsurface attenuated backscatter coefficient (β, $m^{-1}sr^{-1}$) and total and particulate backscattering coefficients (b_b and b_{bp}, m^{-1}). These lidar-derived properties are then validated using autonomous biogeochemical Argo float profiles (Argo, 2020; Claustre, 2010; Organelli et al., 2017) (Text S3) and MODIS ocean color records (NASA, 2018) (Text S4).

2. CALIOP New Global Ocean Subsurface Results

2.1. CALIOP Data and Methods

The CALIOP lidar was designed to provide the observations necessary for an improved understanding of the impact of clouds and aerosols on the Earth's radiation budget and climate (Winker et al., 2010). Since its launch, newly developed applications of CALIOP data for plankton retrievals (Behrenfeld et al., 2013, 2016, 2019; Lu et al., 2014) on the global scale, including high latitude regions during polar nights, have provided the first glimpse into a "new lidar era in satellite oceanography" (Dionisi et al., 2020; Hostetler et al., 2018; Jamet et al., 2019).

However, nonideal polarization separation by the optical components in the CALIOP receiver can cause a small fraction of the backscattered optical power polarized parallel to the receiver reference plane to be misdirected into the perpendicular channel and vice versa (Hostetler et al., 2006). This effect, known as polarization crosstalk, typically causes the measured cross-polarized (i.e., perpendicular channel) attenuated backscatter coefficient ($\beta'_{\perp}$, $m^{-1}sr^{-1}$) to be higher than its true value and the measured co-polarized (i.e., parallel channel) attenuated backscatter coefficient ($\beta'_{\parallel}$, $m^{-1}sr^{-1}$) to be lower than its true value. The relative errors in the CALIOP measured cross-polarized attenuated backscatter coefficient $\left(\frac{\beta'_{\perp,\text{measured}} - \beta'_{\perp,\text{correct}}}{\beta'_{\perp,\text{correct}}} \times 100\%\right)$ due to crosstalk can be up to 100% or more (Text S1) (Lu, Hu, Omar, et al., 2021), which in turn will introduce biases into the subsequently derived ocean optical properties, such as particulate backscattering coefficient (b_{bp}), phytoplankton biomass (C_{phyto}), total particulate organic carbon (POC) stocks, etc. For example, a 0.5% polarization crosstalk can cause ~50% errors on $\beta'_{\perp,\text{measured}}$

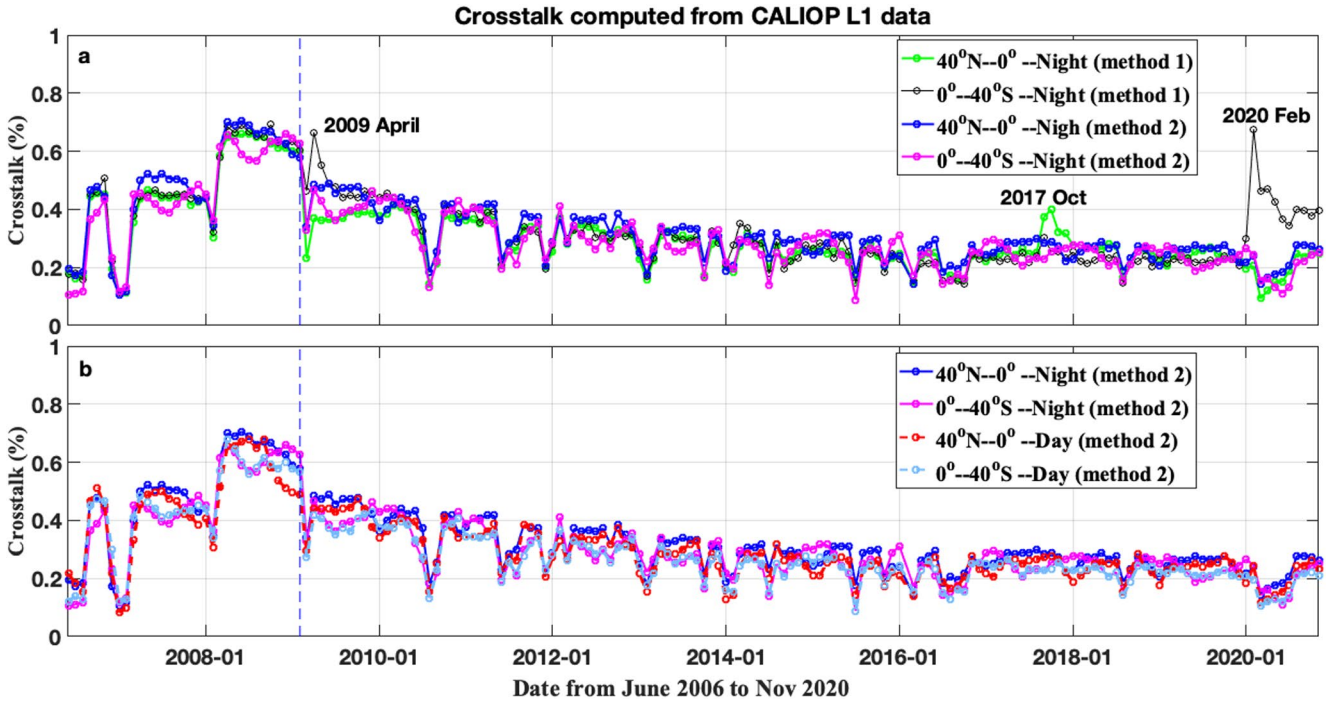

Figure 1. (a) Time series of crosstalk (CT) calculated from Cloud-Aerosol Lidar with Orthogonal Polarization (CALIOP) L1 data by two methods from June 2006 to November 2020 over two chosen regions: 0°–40°N and 0°–40°S. The dashed blue line indicates when CALIOP switched from the primary laser to the backup laser (i.e., February 2009). The discrete jumps in April 2009, September/October 2017, and February 2020 by method 1 are most likely due to the depolarizing smoke injected into the stratosphere; see details in Lu, Hu, Omar, et al. (2021). (b) Crosstalk values during both night and day calculated using method 2.

and total depolarization ratio ($\beta'_{\perp,\text{measured}}/\beta'_{\parallel,\text{measured}}$), and ~59% relative errors of b_{bp}, which yield the errors of CALIOP retrieved C_{phyto} and *POC* of ~59% and ~55%, respectively (Lu, Hu, Omar, et al., 2021). Consequently, estimates of ocean optical properties from CALIOP measurements must take crosstalk into account. Previous analyses of CALIOP L1 data for ocean properties' retrievals (Dionisi et al., 2020; Lacour et al., 2020; Lu et al., 2014) would be expected to exhibit high crosstalk-induced errors if the effect of optical crosstalk between the 532 nm co-polarized and cross-polarized channels was ignored. The global distributions of b_{bp} and total depolarization ratio before and after crosstalk correction given in the work of Lu, Hu, Omar, et al. (2021) indicate that the crosstalk induced error in depolarization ratio and b_{bp} can be as large as 100% between roughly 40°N and 40°S. As a result, using CALIOP crosstalk-corrected signals is highly recommended for all future ocean subsurface studies. The new CALIOP ocean subsurface results reported in this paper are corrected for the crosstalk effect.

Detailed descriptions of two approaches for estimating the polarization crosstalk (CT) between CALIOP's 532 nm parallel and perpendicular channels are given in the work of Lu, Hu, Omar, et al. (2021). Briefly, crosstalk magnitudes can be estimated from the clear air depolarization ratios measured between 20 and 30 km (method 1) and from the ocean surface backscatter signals in the parallel and perpendicular channels (method 2). The two methods for estimating CALIOP crosstalk are completely independent. Figure 1a shows the time series of nighttime crosstalk values calculated from CALIOP L1 data by the two methods from June 2006 to November 2020 over two chosen regions: 0°–40°N and 0°–40°S. Similarly, comparisons of the crosstalk computed during both night and day through method 2 are shown in Figure 1b. The relative differences of the crosstalk values within the two chosen regions and computed by the two different methods are less than 10%, with the root mean square (RMS) of differences ~0.04%. The mean difference of crosstalk between day and night shown in Figure 1b is less than 5% with RMS ~0.03%. The results shown in Figure 1, computed in two different regions and by two independent methods, indicate that the CALIOP crosstalk is correctly and accurately characterized (Lu, Hu, Omar, et al., 2021).

The proposed crosstalk correction method in the work of Lu, Hu, Omar, et al. (2021) has been used to correct CALIOP's measurements of attenuated backscatter coefficients at the near surface of the Earth's oceans as

$$\beta'_{\parallel,\text{correct}}(z) = \frac{\beta'_{\parallel,\text{measured}}(z)}{1-\text{CT}} \tag{1}$$

$$\beta'_{\perp,\text{correct}}(z) = \beta'_{\perp,\text{measured}}(z) - \text{CT} \times \beta'_{\parallel,\text{correct}}(z) \tag{2}$$

The signals of interest can then be derived from the corrected measurement signals in a straightforward manner, with the magnitudes of the crosstalk shown in Figure 1 being used in Equations 1 and 2. The cross-polarization component of ocean subsurface backscatter (β_{w+}, sr^{-1}), particulate backscattering coefficient (b_{bp}, m^{-1}), total (δ_{total}), and subsurface (δ_{sub}) depolarization ratio are obtained from CALIOP crosstalk-corrected ocean attenuated backscatter coefficients ($\beta'_{\parallel,\text{correct}}$,$\beta'_{\perp,\text{correct}}$) as:

$$\beta_{w+} = \frac{\delta_{\text{total}}\beta_s}{1-10\delta_{total}} \tag{3}$$

$$\delta_{\text{total}} = \frac{\sum_{z(pi-1)}^{z(pi+3)}\beta'_{\perp,\text{correct}}(z)}{\sum_{z(pi-1)}^{z(pi+3)}\beta'_{\parallel,\text{correct}}(z)} \tag{4}$$

$$\delta_{\text{sub}} = \frac{\beta_{w+}}{Rrs-\beta_{w+}} \tag{5}$$

$$b_{bp} = \frac{\beta_{w+}}{\tilde{\beta}(\pi)\times t^2} \tag{6}$$

where p_i indicates the altitude index of the peak ocean surface return bin and β_s is the theoretical ocean surface backscatter estimated from wind speed (Y. Hu et al., 2008; Lu et al., 2014). The AMSR-E (2008–2011) and Modern-Era Retrospective Analysis for Research and Applications-version 2 (MERRA-2) (2011–2020) wind speeds were used in this paper (Text S5). $\tilde{\beta}(\pi)$ (sr^{-1}) is the particulate phase function in the backward direction (Lu et al., 2016; J. Sullivan & Twardowski, 2009) and t is the ocean surface transmittance (~0.98 at 532 nm). *Rrs* (sr^{-1}) is the remote sensing reflectance at 531 nm from MODIS ocean color data (e.g., Figure S1, Text S4).

2.2. Global CALIOP β_{w+}, δ_{sub}, and b_{bp}

After the application of Equations 1–6, the CALIOP data are seasonally averaged for the 2008–2020 period and binnned on a 1° latitude by 1° longitude global grid (Figures 2–6). Unlike the co-polarization signal, which can be contaminated by ocean surface reflection, the β_{w+} is due almost entirely to backscatter from ocean subsurface particulate matter (Behrenfeld et al., 2013; Lu et al., 2016). The new global cross-polarization component of the total ocean subsurface backscatter (β_{w+}, sr^{-1}) during both nighttime (Figure 2) and daytime (Figure 3) exhibits all the major ocean plankton features anticipated from the earlier data record, such as Figure S1 of global ocean remote sensing reflectance at 531 nm from MODIS measurements. The low values of β_{w+} over most of the permanently stratified ocean (roughly between 40°N and 40°S latitudes) are stable over the annual cycle, indicating low nutrient, low biomass waters, except in coastal regions and the Eastern Pacific upwelling region (Behrenfeld et al., 2013). The seasonal changes of β_{w+} (Figures 2a–2d and 3a–3d) illustrate the strong seasonality of high latitude phytoplankton communities. For example, the elevated β_{w+} values in the subarctic oceans reflect the large boreal summer (June–August) phytoplankton bloom (Figures 2b and 3b), while β_{w+} in the Southern Oceans reflect the large austral summer (December–February) bloom (Figures 2d and 3d). The high latitude β_{w+} (Figure 2 vs. Figure 3) also indicates the day–night differences, which is useful for further studies of day–night differences in phytoplankton removal rates (Behrenfeld et al., 2019).

The new CALIOP-derived β_{w+} is a fundamental parameter that can be used as the input to retrieve high-level ocean subsurface properties such as δ_{sub} (Equation 5), b_{bp} (Equation 6), and POC (Behrenfeld et al., 2013; Lu et al., 2014). The lidar-derived depth-integrated backscatter is comparable to ocean color remote sensing reflectance (Lu, Hu, Yang, et al., 2020). The ocean subsurface depolarization ratio (Figure 4) can be derived

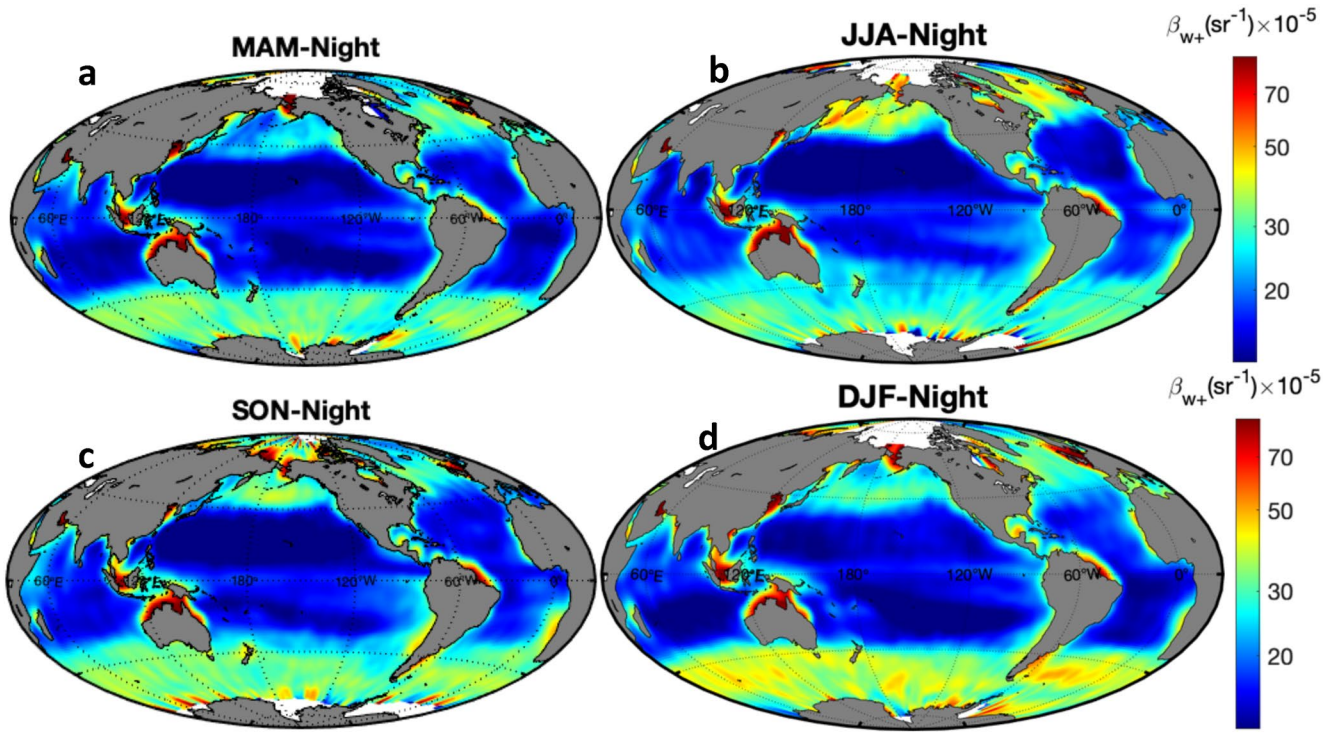

Figure 2. Seasonal distributions of Cloud-Aerosol Lidar with Orthogonal Polarization cross-polarization component of the ocean subsurface backscatter ($\beta_{w+}sr^{-1}$) during nighttime: (a) March–May; (b) June–August; (c) September–November; and (d) December–February. Data are seasonally averaged climatologies for the 2008–2020 period binned to 1° latitude × 1° longitude pixels.

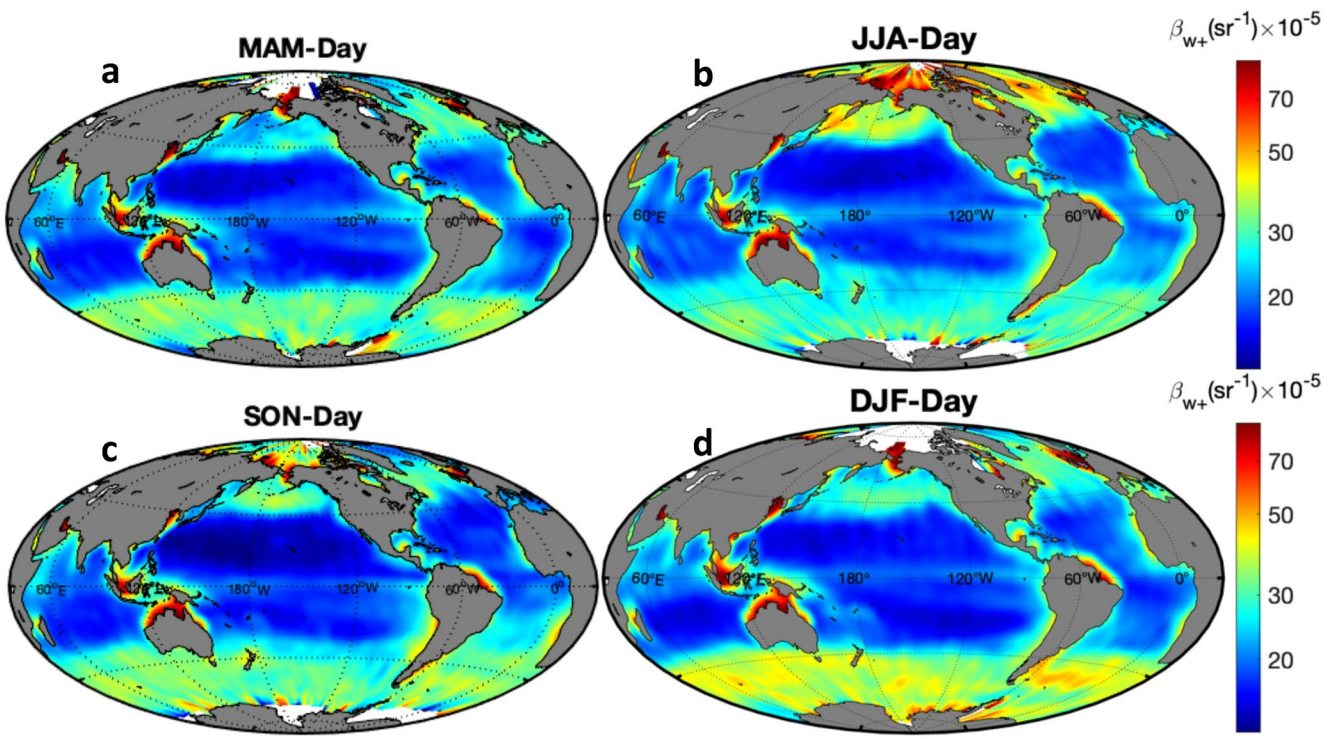

Figure 3. Same as Figure 1 but for daytime results.

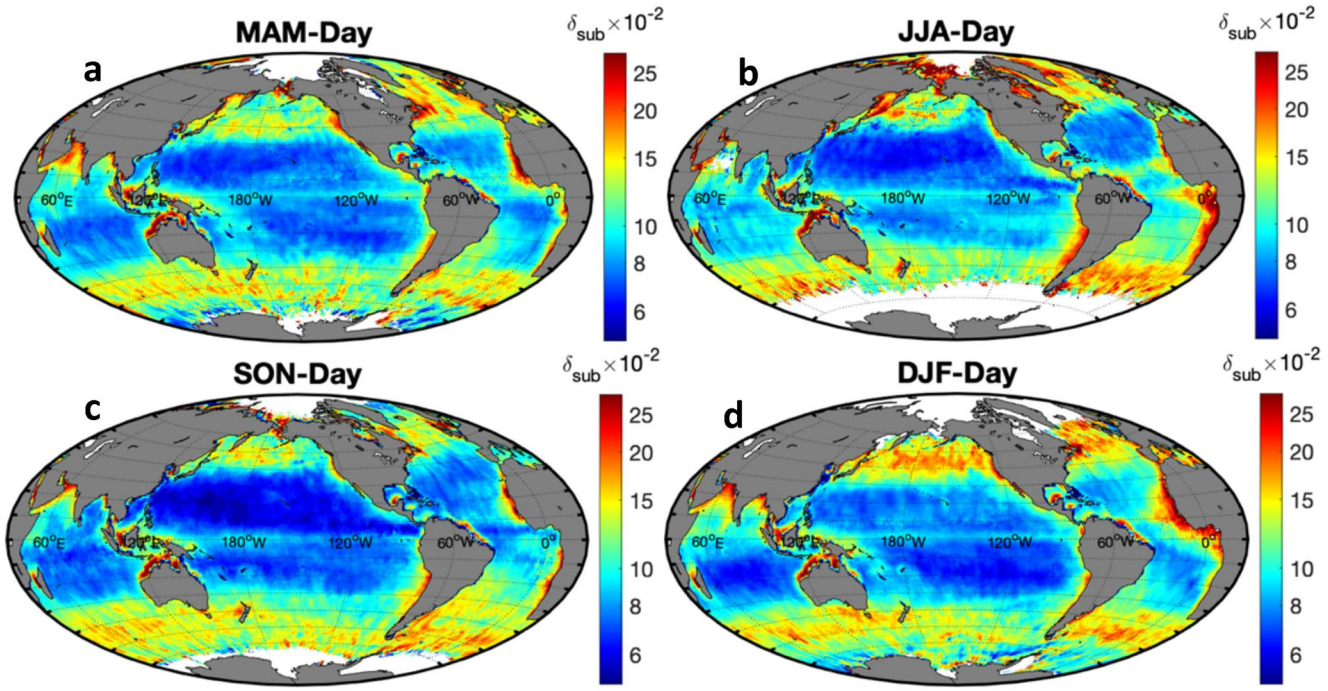

Figure 4. Seasonal distributions of subsurface depolarization ratio (δ_{sub}) during daytime: (a) March–May; (b) June–August; (c) September–November; and (d) December–February. Data are seasonally averaged climatologies for the 2008–2020 period binned to 1° latitude × 1° longitude pixels.

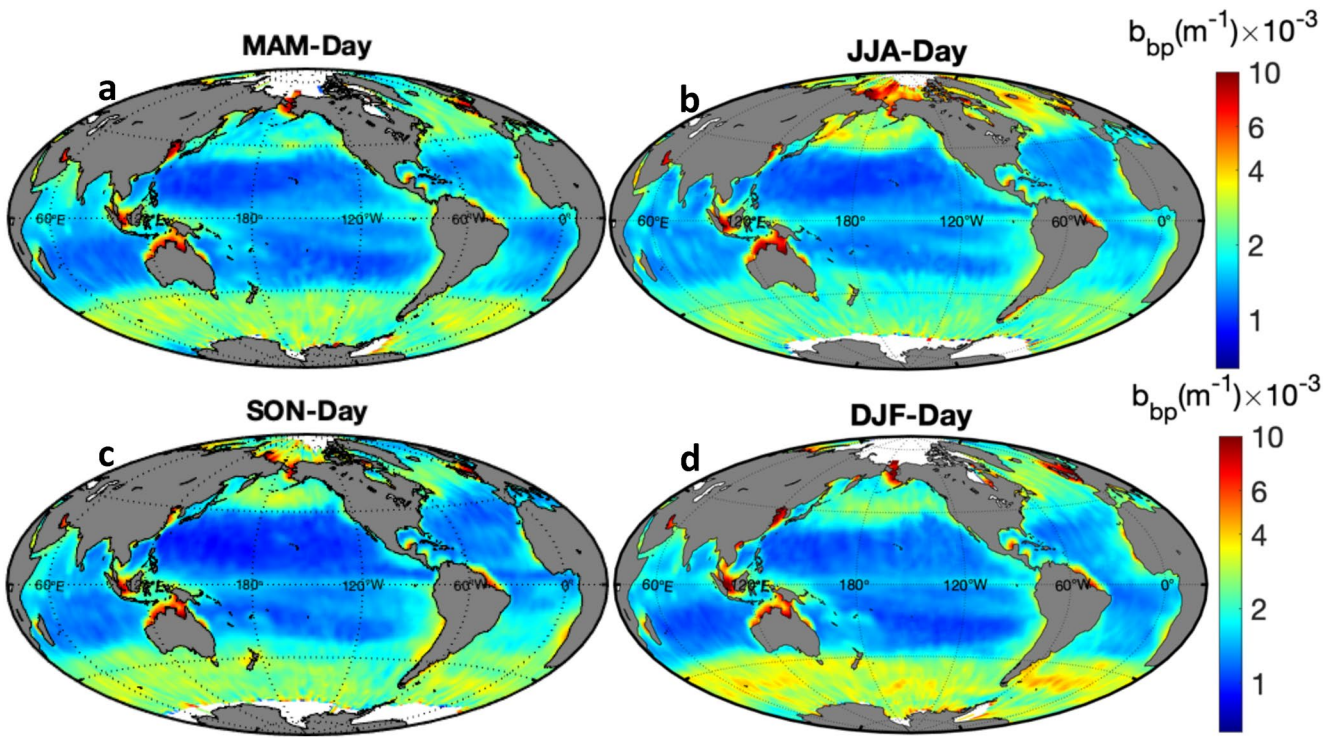

Figure 5. Seasonal distributions of Cloud-Aerosol Lidar with Orthogonal Polarization particulate backscattering coefficient (b_{bp}, m^{-1}) after crosstalk corrected during daytime: (a) March–May; (b) June–August; (c) September–November; and (d) December–February. Data are seasonally averaged climatologies for the 2008–2020 period binned to 1° latitude × 1° longitude pixels.

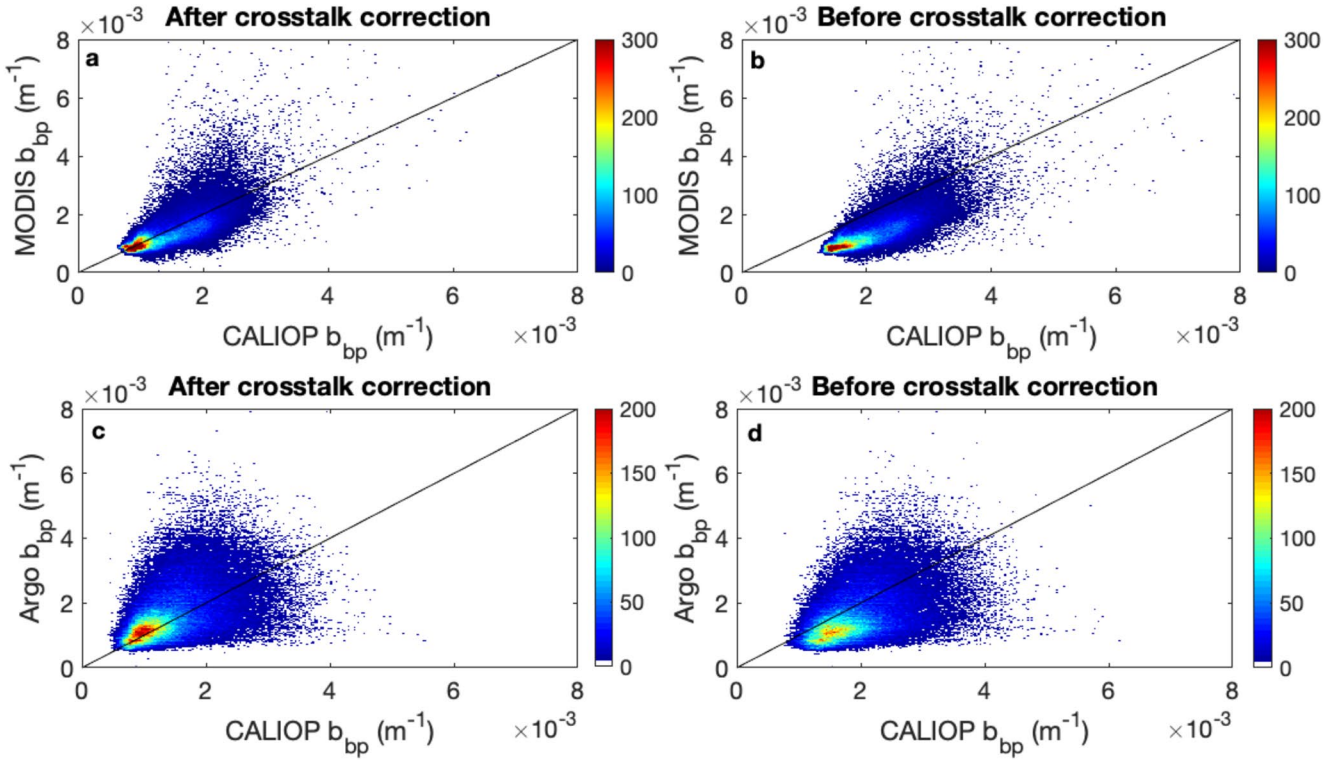

Figure 6. Comparison of b_{bp} from three different sources: Cloud-Aerosol Lidar with Orthogonal Polarization (CALIOP) (*x*-axis) versus MODerate-resolution Imaging Spectroradiometer (*y*-axis) (a and b), CALIOP (*x*-axis) versus Argo float (*y*-axis) (c and d). The color is the number of collocated matchups of 1° by 1° grid boxes from May 2010 to November 2020.

by combining CALIOP β_{w+} data at 532 nm and MODIS remote sensing reflectance (*Rrs*, sr^{-1}) data at 531 nm (Figure S1) as in Equation 5. The difference between the two quantities, *Rrs*–β_{w+}, represents the co-polarization component of the total subsurface backscatter. For comparisons, global seasonal maps of CALIOP-derived total depolarization ratio (Equation 4), including both surface and subsurface contributions, are provided in Figure S2. Due to ocean surface contributions, δ_{total} is less than 0.1 for most of the global ocean. There are very few published measurements of below-surface depolarization ratios, with global spatial and seasonal distributions being especially rare. The newly derived δ_{sub} shown in Figure 4 provides some initial insights into the below-surface particulate matter shape, which should be especially useful for studies of phytoplankton communities and diversity in the global oceans (Righetti et al., 2019; Vallina et al., 2014). Uncertainties in the derivation of δ_{sub} depend on the calibration of both CALIOP β_{w+} and MODIS *Rrs*. Assuming a 10% uncertainty for MODIS *Rrs* (C. Hu et al., 2013) and CALIOP β_{w+}, the uncertainty of δ_{sub} is ~14%.

The global distributions of CALIOP-derived b_{bp} (m^{-1}), retrieved using Equation 6 and crosstalk-corrected values of β_{w+} from Equation 3, are given in Figure 5. For comparison, the CALIOP-derived b_{bp} (m^{-1}) without crosstalk corrections are shown in Figure S3 . To validate the crosstalk corrections applied to the CALIOP-derived b_{bp} at 532 nm, we used in situ b_{bp} measurements by autonomous profiling Argo floats (Figure S5 and Text S3) and MODIS-Aqua monthly ocean color b_{bp} products (Text S4) from May 2010 to November 2020. CALIOP, MODIS, and Argo float b_{bp} results were binned over 1° by 1° grid boxes and monthly time periods.

The seasonal distributions of Argo float b_{bp} at 532 nm are given in Figure S4. The Argo float (e.g., Figure S4) and CALIOP (Figure 5) b_{bp} results reflect the large Boreal summer (June–August) phytoplankton bloom in the subarctic oceans and the large Austral summer (December–February) bloom in the Southern Oceans. Figure 6 shows the b_{bp} comparisons from three different sources: CALIOP versus MODIS (a and b) and CALIOP versus Argo float (c and d). The CALIOP b_{bp} values in Figures 6a and 6c have been corrected for polarization crosstalk. In contrast, crosstalk corrections were not applied to the CALIOP b_{bp} values in

Figures 6b and 6d. Table S1 provides the performance indices of CALIOP b_{bp} estimates before and after crosstalk correction. The comparisons in Figure 6 and Table S1 indicate that (a) the CALIOP-derived b_{bp} before crosstalk correction are higher than MODIS and Argo float b_{bp} results because the crosstalk causes the measured β_{w+} to be higher than its true value, and (b) the CALIOP derived b_{bp} after crosstalk correction shows substantially better agreement with both MODIS b_{bp} (Figure 6a) and Argo float b_{bp} (Figure 6c) results.

3. ATLAS Ocean Subsurface High Vertical Resolution Profiles

3.1. ATLAS Data and Methods

ICESat-2 is a follow-on to the original ICESat mission (Abshire et al., 2005) that provides global altimetry and atmospheric measurements with particular emphasis on surface elevation changes in the polar regions (Markus et al., 2017). ATLAS uses photomultiplier tubes as detectors in the photon-counting mode so that a single photon reflected back to the receiver triggers a detection within the ICESat-2 data acquisition system. The single-photon-sensitive detection technique used by ATLAS to measure the photon time of flight provides the very high vertical resolution required to detect small spatial and temporal changes in polar ice elevations (Neumann et al., 2019; Popescu et al., 2018). Many other areas of Earth science also benefit from the ICESat-2 mission. For the atmospheric community, ICESat-2 delivers calibrated, attenuated backscatter profiles, cloud and aerosol heights, and column optical depths (Palm et al., 2021). The hydrological community uses ICESat-2 measurements to determine global inland water body heights and associated properties (Jasinski et al., 2016). Similarly, the oceanography community can readily obtain shallow water bathymetry and global ocean and wave heights (Morison et al., 2019).

In addition, the ICESat-2-detected photon events over ocean regions provide great opportunity for ocean subsurface studies (Lu et al., 2019; Lu, Hu, Yang, et al., 2020). Details on ocean subsurface properties retrieval methods, including a dedicated deconvolution method to remove ICESat-2 after pulsing effects (e.g., Figure S6), are given in the work of Lu, Hu, Vaughan, et al. (2020), Lu, Hu, Yang, et al. (2020), Lu, Hu, Yang, et al. (2021) and Text S2. Figure S7 gives the concept and schematic flow chart of applying ICESat-2 ATL03 data for ocean subsurface optical properties' retrieval. Briefly, the theoretical ocean surface backscatter at 532 nm is estimated from wind speed (Y. Hu et al., 2008). Then, the calibration coefficients for lidar profiles are the ratios between the theoretical ocean surface backscatter and ATLAS measured photon counts from sea surface. Finally, the profiles of ocean subsurface attenuated backscatter coefficients (e.g., Figure 7a) are the ATLAS measured subsurface photon counts calibrated by the calibration coefficients. The water optical properties of diffuse attenuation coefficient kd (m^{-1}) and total backscattering coefficient b_b (m^{-1}) are retrieved from the profiles of subsurface attenuated backscatter coefficients (Lu, Hu, Yang, et al., 2020).

The new ocean subsurface results (e.g., Figure 7) from the ICESat-2 mission reveal high vertical resolution of subsurface ocean optical properties through the water column that are not available from passive ocean color records or from CALIOP active measurements. The ICESat-2 data thus provide a wealth of unique information to complement existing satellite-based ocean color remote sensing capabilities by adding high spatial and vertical resolution profile measurements during both day and night.

3.2. Evaluation of ATLAS/ICESat-2 Ocean Results

In situ measurements by autonomous profiling Argo floats (Argo, 2020; Claustre, 2010; Organelli et al., 2017) and MODIS-Aqua monthly ocean color products (NASA, 2018) from October 2018 to November 2020 are used to evaluate the ICESat-2-derived ocean results. Details about the Argo float b_{bp} data, MODIS ocean color products, and ICESat-2 ATL03 data used in this paper are provided in Supporting Information S1.

The two-dimensional distributions of (a) attenuated backscatter coefficient ($\beta(z)$, $m^{-1}sr^{-1}$) and (b) total backscattering coefficient ($b_b(z)$) obtained from ICESat-2 measurement on March 5, 2019 are given in Figure 7. The corresponding ICESat-2 ground tracks (green line) and Argo float location (9.32°S, 141°W) on March 5, 2019 are shown in Figure S5. The horizontal distance between Argo float (red star in Figure S5) and ICESat-2 ground track (black line in Figure 7) is ~4.4 km. The seawater backscattering coefficient profile (b_{bw}, m^{-1}) at 532 nm (green dashed line in Figure 8) is obtained based on the Argo float's temperature and salinity profiles (Werdell et al., 2013). The ICESat-2 vertical profile of subsurface particulate backscattering

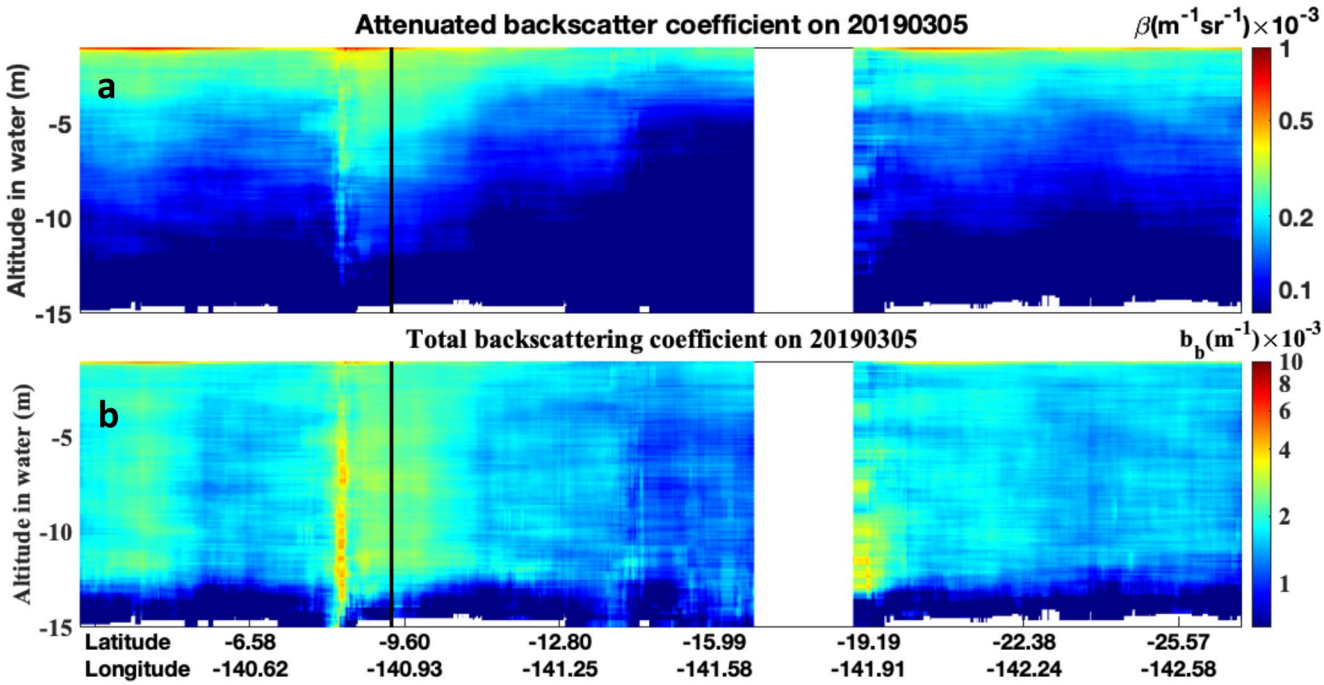

Figure 7. Two-dimensional distributions of (a) attenuated backscatter coefficient (β, $m^{-1}sr^{-1}$) and (b) total backscattering coefficient below ocean surface (b_b, m^{-1}) on March 5, 2019. The *x*-axis specifies locations along Ice, Cloud, and land Elevation Satellite-2 ground tracks (blue line in Figure S5) and *y*-axis is ocean penetration depth in meters. The color bars on the right-hand side provide the range of β and b_b values.

coefficients, $b_{bp}(z)$ (blue in Figure 8), corresponding to the vertical black line in Figure 7 is obtained by subtracting the seawater backscattering coefficient (green dashed line in Figure 8) from the total backscattering coefficient (black line in Figure 7b). Figure 8 shows the vertical profiles of $b_{bp}(z)$ from both the Argo floats and the ICESat-2 measurements on March 5, 2019. The relative differences between the two b_{bp} profiles, $\left(\frac{b_{bp,\,\mathrm{ICESat2}} - b_{bp,\,\mathrm{Argo}}}{b_{bp,\,\mathrm{Argo}}} \times 100\%\right)$, are less than 10%.

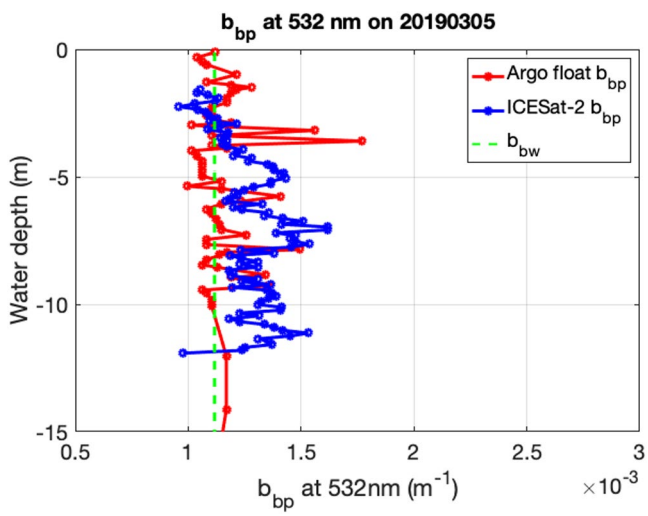

Figure 8. Vertical profiles of particulate backscattering coefficient below ocean surface (b_{bp}, m^{-1}) on March 5, 2019 from Ice, Cloud, and land Elevation Satellite-2 (ICESat-2) (blue) and Argo float (red). The ICESat-2 profile is located at the black line in Figure 4. The distance between black line and Argo float is ~4.4 km (Figure S5). The green dashed line is the seawater backscattering coefficient profile (b_{bw}, m^{-1}) at 532 nm calculated based on Argo float's temperature and salinity vertical profiles on March 5, 2019 at (9.32°S, 141°W).

In order to compare with colocated MODIS ocean color results (i.e., layer-integrated results), the retrieved ICESat-2 profiles of Figure 7 are depth-averaged following the method in the work of Lu, Hu, Yang, et al. (2020) to get layer-integrated ocean subsurface-attenuated backscatter (Rrs, sr^{-1}) and b_b. The diffuse attenuation coefficient, *kd* (m^{-1}), is derived from the exponential decay of the attenuated backscatter profiles, as illustrated in Figure 1 in the work of Lu, Hu, Yang, et al. (2020). Figure S9 shows the comparison between ICESat-2 derived ocean results on March 5, 2019 and colocated MODIS monthly ocean color results in March 2019. Close coincidences between the Aqua and ICESat-2 orbit tracks are infrequent. To overcome the sampling biases engendered by the lack of daily MODIS measurements collocated with ICESat-2 profiles, the monthly MODIS ocean color results are used in this work and the available ICESat-2 profiles are colocated with the nearest 4 × 4 km monthly MODIS pixel. The mean relative differences of *kd* (m^{-1}), b_b, and *Rrs* between ICESat-2 and MODIS measurements are ~7% (Figure S9a), ~38% (Figure S9b), and ~18% (Figure S9c), respectively. The error sources contributing to these differences include the time offset, the different measurement locations (up to 10 km) between ICESat-2 (daily) and MODIS (monthly), the calibration error of lidar ocean surface backscatter from

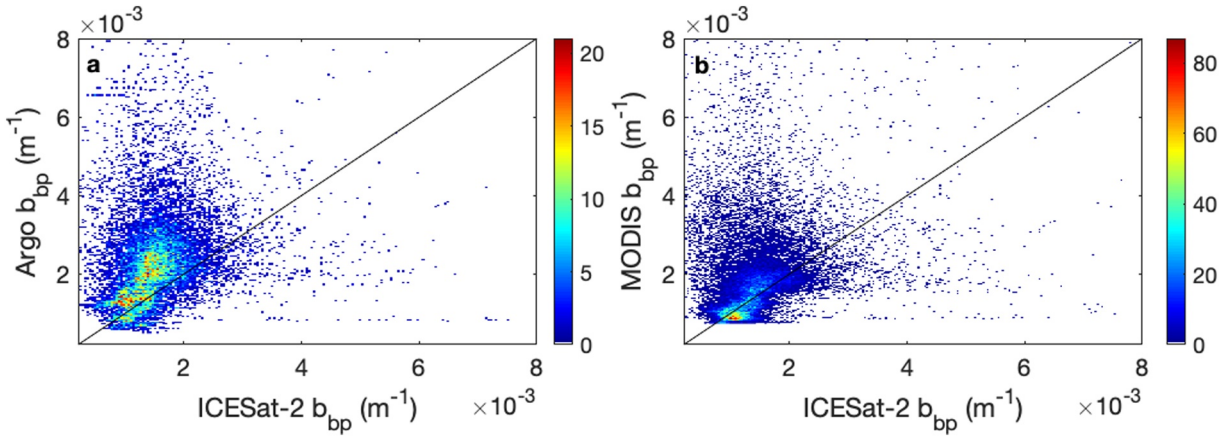

Figure 9. Comparisons of b_{bp} (a) Ice, Cloud, and land Elevation Satellite-2 (ICESat-2) versus Argo float, (b) ICESat-2 versus MODerate-resolution Imaging Spectroradiometer from October 2018 to November 2020. The color is the number of collocated matchups of 1° by 1° grid boxes.

wind speed (Lancaster et al., 2005), and uncertainties and biases associated with MODIS ocean color results (Mélin et al., 2016). The results over the Indian Ocean (Figures S10–S12 and Table S2) from October 2018 to July 2020 indicate that the mean relative differences between ICESat-2 and MODIS are ~11%, ~10%, and ~27% for *kd*, b_b, and *Rrs*, respectively.

While ICESat-2 has very high vertical and along-track spatial resolutions, it does not provide the extensive horizontal spatial coverage delivered by the MODIS images. To enable informative comparisons between these disparate data sets, both ICESat-2 (Figure S8) and MODIS b_{bp} were averaged over 1-month periods and binned on a 1° × 1° grid whenever collocated Argo float b_{bp} results were available (Figures S4 and S5). The seasonal distributions of ICESat-2-retrieved layer-integrated b_{bp} at 532 nm (Lu, Hu, Yang, et al., 2020) from October 2018 to November 2020 are given in Figure S8. The Argo float b_{bp} 1° × 1° results (Figure S4 and Text S3) are colocated with the ICESat-2 1° × 1° pixel. The b_{bp} comparisons between ICESat-2 (Figure S8) and Argo floats (Figure S4) within 1° × 1° pixels are given in Figure 9a. The results indicate that the relative differences between the two b_{bp} data sets are ~22% with an RMS error of ~1.5×10^{-3} m^{-1} (Table S1). The b_{bp} comparisons between ICESat-2 and MODIS ocean color within 1° by 1° pixel are given in Figure 9b. The relative bias between the ICESat-2 and MODIS b_{bp} retrievals is ~9% with an RMS error of ~1.1×10^{-3} m^{-1} (Table S1). Note that MERRA-2 wind speeds are used to calibrate ICESat-2 observed photons from the ocean surface from October 2018 to November 2020 (Y. Hu et al., 2008; Lu, Hu, Yang, et al., 2020), and hence the ICESat-2 calibration accuracy depends on the accuracy of the MERRA-2 wind speed. An accuracy assessment of the MERRA-2 wind speeds lies well beyond the scope of this study.

4. Conclusions

New ocean subsurface optical properties are obtained from two space-based lidars: CALIOP/CALIPSO and ATLAS/ICESat-2. For both lidars, measurement artifacts are removed before retrieving ocean optical properties. Our study is one of many parallel efforts aimed at maximizing the ocean subsurface information that can be uniquely obtained from space-based active remote sensing measurements. As an example, to take full advantage of the capabilities of CALIOP we are currently conducting a study to estimate the co-polarization component of the total subsurface backscatter from CALIOP co-polarization channel, where the ocean surface contribution to co-polarization signal magnitude will be estimated from 1,064 nm channels. Upon successful conclusion of this effort, we expect to provide global ocean subsurface depolarization ratios during nighttime. Additionally, several different research groups are actively exploring the use of ICESat-2 measurements to characterize ocean subsurface properties on global scales. Our expectation is that in situ data from Argo floats and MODIS ocean color results will undoubtedly contribute substantially in future validation efforts.

In addition to the ocean color observations provided by space-based passive sensors over the last few decades, the ocean community can now expect to have more than a decade of ocean records from both CALIOP/CALIPSO (already on orbit for over 15 years) and ATLAS/ICESat-2. The global scale CALIOP retrievals and high vertical resolution ATLAS profiles each provide new and unique information that augment the existing ocean color records acquired by passive remote sensors. This pioneering use of space-based lidars to retrieve ocean subsurface properties will provide a meaningful satellite lidar record to the ocean sciences community and can help the community to assess the complex interactions involving ocean biology, the cryosphere, and the atmosphere. Moreover, the satellite lidar record will provide important preparatory data for the upcoming Plankton, Aerosol, Cloud, ocean Ecosystem mission.

Conflict of Interest

The authors declare no conflicts of interest relevant to this study.

Data Availability Statement

The CALIPSO V4.10 lidar level 1B profile data used in this study can be freely accessed at https://doi.org/10.5067/CALIOP/CALIPSO/LID_L1-Standard-V4-10. The ICESat-2 data are publicly available through the National Snow and Ice Data Center (NSIDC). The geolocated photon data (ATL03 Release 003) can be found online (https://nsidc.org/data/atl03). Data sets for this research are available in these in-text data citation references: Neumann et al. (2020). The MODIS ocean color data can be freely downloaded from NASA Ocean Color Data Web (http://oceandata.sci.gsfc.nasa.gov accessed on March 23, 2021). The Argo floats data were collected by the International Argo Program and the national programs and are freely available at http://www.coriolis.eu.org/Data-Products/Data-Delivery/Data-selection or freely available from the FTP site: ftp://ftp.ifremer.fr/ifremer/argo/dac/. The AMSR-E wind speeds are available freely through NSIDC (https://n5eil01u.ecs.nsidc.org/AMSA/AE_MoOcn.002/), and MERRA-2 wind speeds can be obtained from the Global Modeling and Assimilation office at https://gmao.gsfc.nasa.gov/reanalysis/MERRA-2/, accessed on March 23, 2021.

Acknowledgments
The authors would like to thank the NASA CALIPSO, ICESat-2, and MODIS teams for providing the data used in this study. Funding for the lead author was provided by the NASA awards (grant numbers 80NSSC20K0129 and 80NSSC21K0910) for CALIPSO and ICESat-2 projects.

References

Abshire, J. B., Sun, X., Riris, H., Sirota, J. M., McGarry, J. F., Palm, S., et al. (2005). Geoscience Laser Altimeter System (GLAS) on the ICESat Mission: On-orbit measurement performance. *Geophysical Research Letters*, *32*(21). https://doi.org/10.1029/2005GL024028

Argo. (2020). *Argo float data and metadata from Global Data Assembly Centre (Argo GDAC)*. SEANOE. https://doi.org/10.17882/42182

Behrenfeld, M. J., Gaube, P., Della Penna, A., O'Malley, R. T., Burt, W. J., Hu, Y., et al. (2019). Global satellite-observed daily vertical migrations of ocean animals. *Nature*, *576*(7786), 257–261. https://doi.org/10.1038/s41586-019-1796-9

Behrenfeld, M. J., Hu, Y., Hostetler, C. A., Dall'Olmo, G., Rodier, S. D., Hair, J. W., & Trepte, C. R. (2013). Space-based lidar measurements of global ocean carbon stocks. *Geophysical Research Letters*, *40*(16), 4355–4360. https://doi.org/10.1002/grl.50816

Behrenfeld, M. J., Hu, Y., O'Malley, R. T., Boss, E. S., Hostetler, C. A., Siegel, D. A., et al. (2016). Annual boom-bust cycles of polar phytoplankton biomass revealed by space-based lidar. *Nature Geoscience*, *10*, 118–122. https://doi.org/10.1038/ngeo2861

Behrenfeld, M. J., Hu, Y., O/'Malley, R. T., Boss, E. S., Hostetler, C. A., Siegel, D. A., et al. (2017). Annual boom-bust cycles of polar phytoplankton biomass revealed by space-based lidar. *Nature Geoscience*, *10*(2), 118–122. https://doi.org/10.1038/ngeo2861

Blondeau-Patissier, D., Gower, J. F. R., Dekker, A. G., Phinn, S. R., & Brando, V. E. (2014). A review of ocean color remote sensing methods and statistical techniques for the detection, mapping and analysis of phytoplankton blooms in coastal and open oceans. *Progress in Oceanography*, *123*, 123–144. https://doi.org/10.1016/j.pocean.2013.12.008

Brown, O. B., Evans, R. H., Brown, J. W., Gordon, H. R., Smith, R. C., & Baker, K. S. (1985). Phytoplankton blooming off the U.S. east coast: A satellite description. *Science*, *229*(4709), 163–167. https://doi.org/10.1126/science.229.4709.163

Churnside, J., McCarty, B., & Lu, X. (2013). Subsurface ocean signals from an orbiting polarization lidar. *Remote Sensing*, *5*(7), 3457–3475. https://doi.org/10.3390/rs5073457

Claustre, H. (2010). *Bio-optical profiling floats as new observational tools for biogeochemical and ecosystem studies: Potential synergies with ocean color remote sensing* (pp. 177–183). Lawrence Berkeley National Laboratory.

Dickey, T., Lewis, M., & Chang, G. (2006). Optical oceanography: Recent advances and future directions using global remote sensing and in situ observations. *Reviews of Geophysics*, *44*(1). https://doi.org/10.1029/2003RG000148

Dionisi, D., Brando, V. E., Volpe, G., Colella, S., & Santoleri, R. (2020). Seasonal distributions of ocean particulate optical properties from spaceborne lidar measurements in Mediterranean and Black sea. *Remote Sensing of Environment*, *247*, 111889. https://doi.org/10.1016/j.rse.2020.111889

Getzewich, B. J., Vaughan, M. A., Hunt, W. H., Avery, M. A., Powell, K. A., Tackett, J. L., et al. (2018). CALIPSO lidar calibration at 532 nm: Version 4 daytime algorithm. *Atmospheric Measurement Techniques*, *11*(11), 6309–6326. https://doi.org/10.5194/amt-11-6309-2018

Hostetler, C. A., Behrenfeld, M. J., Hu, Y., Hair, J. W., & Schulien, J. A. (2018). Spaceborne lidar in the study of marine systems. *Annual Review of Marine Science*, *10*(1), 121–147. https://doi.org/10.1146/annurev-marine-121916-063335

Hostetler, C. A., Liu, Z., Reagan, J., Vaughan, M., Winker, D., Osborn, M., et al. (2006). *CALIOP algorithm theoretical basis document calibration and level 1 data products* (PC-SCI-201 Release 1.0). Retrieved from https://www-calipso.larc.nasa.gov/resources/pdfs/PC-SCI-201v1.0.pdf

Hovis, W. A., Clark, D. K., Anderson, F., Austin, R. W., Wilson, W. H., Baker, E. T., et al. (1980). Nimbus-7 coastal zone color scanner: System description and initial imagery. *Science*, *210*(4465), 60–63. https://doi.org/10.1126/science.210.4465.60

Hu, C., Feng, L., & Lee, Z. (2013). Uncertainties of SeaWiFS and MODIS remote sensing reflectance: Implications from clear water measurements. *Remote Sensing of Environment*, *133*, 168–182. https://doi.org/10.1016/j.rse.2013.02.012

Hu, Y., Powell, K., Vaughan, M., Tepte, C., Weimer, C., Beherenfeld, M., et al. (2007). Elevation information in tail (EIT) technique for lidar altimetry. *Optics Express*, *15*(22), 14504–14515. https://doi.org/10.1364/OE.15.014504

Hu, Y., Stamnes, K., Vaughan, M., Pelon, J., Weimer, C., Wu, D., et al. (2008). Sea surface wind speed estimation from space-based lidar measurements. *Atmospheric Chemistry and Physics*, *8*(13), 3593–3601. https://doi.org/10.5194/acp-8-3593-2008

Hunt, W. H., Winker, D. M., Vaughan, M. A., Powell, K. A., Lucker, P. L., & Weimer, C. (2009). CALIPSO lidar description and performance assessment. *Journal of Atmospheric and Oceanic Technology*, *26*(7), 1214–1228. https://doi.org/10.1175/2009JTECHA1223.1

Jamet, C., Ibrahim, A., Ahmad, Z., Angelini, F., Babin, M., Behrenfeld, M. J., et al. (2019). Going beyond standard ocean color observations: Lidar and polarimetry. *Frontiers in Marine Science*, *6*, 251. https://doi.org/10.3389/fmars.2019.00251

Jasinski, M. F., Stoll, J. D., Cook, W. B., Ondrusek, M., Stengel, E., & Brunt, K. (2016). Inland and near-shore water profiles derived from the high-altitude multiple altimeter beam experimental lidar (MABEL). *Journal of Coastal Research*, *76*(SI), 44–55. https://doi.org/10.2112/si76-005

Kar, J., Vaughan, M. A., Lee, K.-P., Tackett, J. L., Avery, M. A., Garnier, A., et al. (2018). CALIPSO lidar calibration at 532 nm: Version 4 nighttime algorithm. *Atmospheric Measurement Techniques*, *11*(3), 1459–1479. https://doi.org/10.5194/amt-11-1459-2018

Lacour, L., Larouche, R., & Babin, M. (2020). In situ evaluation of spaceborne CALIOP lidar measurements of the upper-ocean particle backscattering coefficient. *Optics Express*, *28*(18), 26989–26999. https://doi.org/10.1364/OE.397126

Lancaster, R. S., Spinhirne, J. D., & Palm, S. P. (2005). Laser pulse reflectance of the ocean surface from the GLAS satellite lidar. *Geophysical Research Letters*, *32*(22). https://doi.org/10.1029/2005GL023732

Lu, X., Hu, Y., Omar, A., Baize, R., Vaughan, M., Rodier, S., et al. (2021). Global ocean studies from CALIOP/CALIPSO by removing polarization crosstalk effects. *Remote Sensing*, *13*(14), 2769. https://doi.org/10.3390/rs13142769

Lu, X., Hu, Y., Pelon, J., Trepte, C., Liu, K., Rodier, S., et al. (2016). Retrieval of ocean subsurface particulate backscattering coefficient from space-borne CALIOP lidar measurements. *Optics Express*, *24*(25), 29001–29008. https://doi.org/10.1364/OE.24.029001

Lu, X., Hu, Y., Trepte, C., Zeng, S., & Churnside, J. H. (2014). Ocean subsurface studies with the CALIPSO spaceborne lidar. *Journal of Geophysical Research: Oceans*, *119*(7), 4305–4317. https://doi.org/10.1002/2014jc009970

Lu, X., Hu, Y., Vaughan, M., Rodier, S., Trepte, C., Lucker, P., & Omar, A. (2020). New attenuated backscatter profile by removing the CALIOP receiver's transient response. *Journal of Quantitative Spectroscopy and Radiative Transfer*, *255*, 107244. https://doi.org/10.1016/j.jqsrt.2020.107244

Lu, X., Hu, Y., & Yang, Y. (2019). *Ocean subsurface study from ICESat-2 mission*. In 2019 Photonics & Electromagnetics Research Symposium–Fall (PIERS–Fall) (pp. 910–918). https://doi.org/10.1109/PIERS-Fall48861.2019.9021802

Lu, X., Hu, Y., Yang, Y., Bontempi, P., Omar, A., & Baize, R. (2020). Antarctic spring ice-edge blooms observed from space by ICESat-2. *Remote Sensing of Environment*, *245*, 111827. https://doi.org/10.1016/j.rse.2020.111827

Lu, X., Hu, Y., Yang, Y., Vaughan, M., Liu, Z., Rodier, S., et al. (2018). Laser pulse bidirectional reflectance from CALIPSO mission. *Atmospheric Measurement Techniques*, *11*(6), 3281–3296. https://doi.org/10.5194/amt-11-3281-2018

Lu, X., Hu, Y., Yang, Y., Vaughan, M., Palm, S., Trepte, C., et al. (2021). Enabling value added scientific applications of ICESat-2 data with effective removal of afterpulses. *Earth and Space Science*, *8*(6), e2021EA001729. https://doi.org/10.1029/2021EA001729

Magruder, L., & Brunt, K. (2018). Performance analysis of airborne photon-counting lidar data in preparation for the ICESat-2 mission. *IEEE Transactions on Geoscience and Remote Sensing*, *56*(5), 2911–2918. https://doi.org/10.1109/TGRS.2017.2786659

Magruder, L., Brunt, K., & Alonzo, M. (2020). Early ICESat-2 on-orbit geolocation validation using ground-based corner cube retro-reflectors. *Remote Sensing*, *12*, 3653. https://doi.org/10.3390/rs12213653

Markus, T., Neumann, T., Martino, A., Abdalati, W., Brunt, K., Csatho, B., et al. (2017). The Ice, Cloud, and land Elevation Satellite-2 (ICESat-2): Science requirements, concept, and implementation. *Remote Sensing of Environment*, *190*, 260–273. https://doi.org/10.1016/j.rse.2016.12.029

Mélin, F., Sclep, G., Jackson, T., & Sathyendranath, S. (2016). Uncertainty estimates of remote sensing reflectance derived from comparison of ocean color satellite data sets. *Remote Sensing of Environment*, *177*, 107–124. https://doi.org/10.1016/j.rse.2016.02.014

Morison, J., Hancock, D., Dickinson, S., Robbins, J., Roberts, L., Kwok, R., et al. (2019). *ATLAS/ICESat-2 L3A ocean surface height, version 1*. NASA National Snow and Ice Data Center Distributed Active Archive Center. https://doi.org/10.5067/ATLAS/ATL12.001

NASA, O. E. L., Ocean Biology Processing Group, NASA Goddard Space Flight. (2018). *Moderate-Resolution Imaging Spectroradiometer (MODIS) aqua downwelling diffuse attenuation coefficient data*. https://doi.org/10.5067/AQUA/MODIS/L3M/KD/2018

Neumann, T. A., Brenner, A., Hancock, D., Robbins, J., Saba, J., Harbeck, K., et al. (2020). *ATLAS/ICESat-2 L2A global geolocated photon data, version 3*. https://doi.org/10.5067/ATLAS/ATL03.003

Neumann, T. A., Martino, A. J., Markus, T., Bae, S., Bock, M. R., Brenner, A. C., et al. (2019). The Ice, Cloud, and Land Elevation Satellite-2 mission: A global geolocated photon product derived from the Advanced Topographic Laser Altimeter System. *Remote Sensing of Environment*, *233*, 111325. https://doi.org/10.1016/j.rse.2019.111325

Organelli, E., Barbieux, M., Claustre, H., Schmechtig, C., Poteau, A., Bricaud, A., et al. (2017). Two databases derived from BGC-Argo float measurements for marine biogeochemical and bio-optical applications. *Earth System Science Data*, *9*(2), 861–880. https://doi.org/10.5194/essd-9-861-2017

Palm, S., Yang, Y., Herzfeld, U., Hancock, D., Hayes, A., Selmer, P., et al. (2021). ICESat-2 atmospheric channel description, data processing and first results. *Earth and Space Science*, *8*, e2020EA001470. https://doi.org/10.1029/2020EA001470

Popescu, S. C., Zhou, T., Nelson, R., Neuenschwander, A., Sheridan, R., Narine, L., & Walsh, K. M. (2018). Photon counting LiDAR: An adaptive ground and canopy height retrieval algorithm for ICESat-2 data. *Remote Sensing of Environment*, *208*, 154–170. https://doi.org/10.1016/j.rse.2018.02.019

Righetti, D., Vogt, M., Gruber, N., Psomas, A., & Zimmermann, N. E. (2019). Global pattern of phytoplankton diversity driven by temperature and environmental variability. *Science Advances*, *5*(5), eaau6253. https://doi.org/10.1126/sciadv.aau6253

Sullivan, C. W., Arrigo, K. R., McClain, C. R., Comiso, J. C., & Firestone, J. (1993). Distributions of phytoplankton blooms in the Southern Ocean. *Science*, *262*(5141), 1832–1837. https://doi.org/10.1126/science.262.5141.1832

Sullivan, J., & Twardowski, M. S. (2009). Angular shape of the oceanic particulate volume scattering function in the backward direction. *Applied Optics*, *48*(35), 6811–6819. https://doi.org/10.1364/AO.48.006811

Vallina, S. M., Follows, M. J., Dutkiewicz, S., Montoya, J. M., Cermeno, P., & Loreau, M. (2014). Global relationship between phytoplankton diversity and productivity in the ocean. *Nature Communications*, *5*(1), 4299. https://doi.org/10.1038/ncomms5299

Werdell, P. J., Franz, B. A., Lefler, J. T., Robinson, W. D., & Boss, E. (2013). Retrieving marine inherent optical properties from satellites using temperature and salinity-dependent backscattering by seawater. *Optics Express*, *21*(26), 32611–32622. https://doi.org/10.1364/OE.21.032611

Winker, D. M., Vaughan, M. A., Omar, A., Hu, Y., Powell, K. A., Liu, Z., et al. (2009). Overview of the CALIPSO mission and CALIOP data processing algorithms. *Journal of Atmospheric and Oceanic Technology*, *26*(11), 2310–2323. https://doi.org/10.1175/2009jtecha1281.1

Winker, D. M., Pelon, J., Coakley, J. A., Ackerman, S. A., Charlson, R. J., Colarco, P. R., et al. (2010). The CALIPSO mission: A global 3D view of aerosols and clouds. *Bulletin of the American Meteorological Society*, *91*(9), 1211–1230. https://doi.org/10.1175/2010bams3009.1

References From the Supporting Information

Lee, Z., Carder, K. L., & Arnone, R. A. (2002). Deriving inherent optical properties from water color: A multiband quasi-analytical algorithm for optically deep waters. *Applied Optics*, *41*(27), 5755–5772. https://doi.org/10.1364/AO.41.005755

Loisel, H., Nicolas, J.-M., Sciandra, A., Stramski, D., & Poteau, A. (2006). Spectral dependency of optical backscattering by marine particles from satellite remote sensing of the global ocean. *Journal of Geophysical Research*, *111*(C9). https://doi.org/10.1029/2005JC003367

Maritorena, S., Siegel, D. A., & Peterson, A. R. (2002). Optimization of a semianalytical ocean color model for global-scale applications. *Applied Optics*, *41*(15), 2705–2714. https://doi.org/10.1364/AO.41.002705